Bargmann, S.; Reddy, B.D.; Klusemann, B.:

A computational study of a model of single-crystal strain-gradient viscoplasticity with an interactive hardening relation

In: International Journal of Solids and Structures (2014) Elsevier

DOI: 10.1016/j.ijsolstr.2014.03.010

A computational study of a model of single-crystal strain-gradient viscoplasticity with an interactive hardening relation

Swantje Bargmann[1,2], B. Daya Reddy[3], Benjamin Klusemann[1,*]

[1] Institute of Continuum Mechanics and Material Mechanics, Hamburg University of Technology, Germany

[2] Institute of Materials Research, Materials Mechanics, Helmholtz-Zentrum Geesthacht, Max-Planck-Str. 1, 21502 Geesthacht, Germany

[3] Centre for Research in Computational and Applied Mechanics, and Department of Mathematics and Applied Mathematics, University of Cape Town, 7701 Rondebosch, South Africa

∗ Corresponding author. Phone: +49 40 42878 2322, Email: benjamin.klusemann@tu-harburg.de

Abstract The behavior of a model of single-crystal strain-gradient viscoplasticity is investigated. The model is an extension of a rate-independent version, and includes a new hardening relation that has recently been proposed in the small-deformation context [Gurtin and Reddy, 2014], and which accounts for slip-system interactions due to self and latent hardening. Energetic and dissipative effects, each with its corresponding length scale, are included. Numerical results are presented for a single crystal with single and multiple slip systems, as well as an ensemble of grains. These results provide a clear illustration of the effects of accounting for slip-system interactions.

1 Introduction

The hardening behavior of a crystalline metal depends on a number of factors such as elastic stiffness, strength, dislocation interaction, etc., as well as on the grain size (see for example [27, 41]). In the context of gradient extended crystal plasticity, which is motivated by the size-dependent effects that predominate at the micron scale, theories have been proposed by various authors. The literature on the subject has increasead significantly in the last decade and more, with representative and important works including those by Fleck and Hutchinson, Gurtin and Anand, and Nix and Gao [18, 21, 37, 46].

Recently, within the small-deformation framework, Gurtin and Reddy [26] have introduced a rate-independent, thermodynamically consistent, single-crystal plasticity theory which accounts for self- and latent hardening. The behavior of the new hardening relation, and in particular its comparison with other hardening laws that have been in use for some time, have been studied by Povall et al. [42] for the conventional (that is, non-gradient) theory. These authors show via selected numerical examples that, while the slip resistances as proposed by the different theories

vary quite considerably, the overall response of single crystals when subjected to various loading conditions is qualitatively similar for the different models. Other recent contributions that deal with self- and latent hardening include works by Bardella [8], Bargmann et al. [12], Conti and Ortiz [14], Evers et al. [17], Klusemann et al. [31], Levkovitch and Svendsen [33], Wulfinghoff and Böhlke [48], Yalcinkaya et al. [49].

The Gurtin-Reddy model [26] has the advantage of simplicity: it is defined as a function of the generalized accumulated slips, while established models such as that due to Pierce, Asaro and Needleman [40] are defined implicitly via a system of differential equations. The purpose of this contribution is essentially to extend the work carried out in [42], by investigating computationally the behavior of the model of interactive slip resistances, for the strain-gradient theory. This is done in a large-deformation context, and for a viscoplastic extension of the model presented in [26].

2 Basic kinematics: Single crystal plasticity

In large-deformation plasticity, the main assumption is the classical multiplicative split of the deformation gradient $\boldsymbol{F}$ into an elastic $\boldsymbol{F}_{\mathrm{e}}$ and a plastic part $\boldsymbol{F}_{\mathrm{p}}$:

$$\boldsymbol{F} = \boldsymbol{F}_{\mathrm{e}} \cdot \boldsymbol{F}_{\mathrm{p}} \,. \tag{1}$$

The plastic part $\boldsymbol{F}_{\mathrm{p}}$ is assumed to arise due to inelastic slip in the preferred crystallographic planes. The elastic contribution $\boldsymbol{F}_{\mathrm{e}}$ accounts for lattice distortion and rotation. The Green–Lagrange strain and the right Cauchy–Green stretch tensors are defined by

$$\boldsymbol{E} := \frac{1}{2}[\boldsymbol{F}^t \cdot \boldsymbol{F} - \boldsymbol{I}], \qquad \boldsymbol{C} = \boldsymbol{F}^t \cdot \boldsymbol{F} \tag{2}$$

and their elastic counterparts by

$$\boldsymbol{E}_{\mathrm{e}} := \frac{1}{2}[[\boldsymbol{F}_{\mathrm{e}}]^t \cdot \boldsymbol{F}_{\mathrm{e}} - \bar{\boldsymbol{I}}], \qquad \boldsymbol{C}_{\mathrm{e}} = \boldsymbol{F}_{\mathrm{e}}^t \cdot \boldsymbol{F}_{\mathrm{e}}, \tag{3}$$

where $\boldsymbol{I}$ and $\bar{\boldsymbol{I}}$ denote the identity tensors in the reference and intermediate configurations respectively.

2.1 Glide system kinematics

As usual, the crystal plasticity model is based on the glide-system geometry described by the glide direction $\boldsymbol{s}_\alpha$ and glide-plane normal $\boldsymbol{n}_\alpha$, both fixed unit vectors in the intermediate configuration $\mathcal{B}_{\mathrm{i}}$. Together with the direction $\boldsymbol{p}_\alpha = \boldsymbol{n}_\alpha \times \boldsymbol{s}_\alpha$ transverse to $\boldsymbol{s}_\alpha$ in the glide plane,

they form an orthonormal system. It is well known that often two or more crystallographically equivalent systems contribute to the plastic deformation.

In terms of the glide-system geometry, the evolution of the plastic part $\boldsymbol{F}_{\mathrm{p}}$ of the deformation gradient is given in terms of the glide-system geometry and slip rates ν_α by

$$\dot{\boldsymbol{F}}_{\mathrm{p}} = \sum_{\alpha} \nu_\alpha \, \boldsymbol{s}_\alpha \otimes \boldsymbol{F}_{\mathrm{p}}^{t} \cdot \boldsymbol{n}_\alpha \,. \tag{4}$$

Thus, the plastic flow $\boldsymbol{L}_{\mathrm{p}} = \dot{\boldsymbol{F}}_{\mathrm{p}} \cdot \boldsymbol{F}_{\mathrm{p}}^{-1}$ is governed by the slip rates ν_α. Further, it is convenient to define a generalized slip rate $\boldsymbol{\Gamma}_\alpha$ by

$$\boldsymbol{\Gamma}_\alpha = \begin{pmatrix} \nu_\alpha \\ l_{d,\alpha} \nabla_{\boldsymbol{X}} \nu_\alpha \end{pmatrix}, \tag{5}$$

where $l_{d,\alpha}$ is a dissipative length scale associated with slip system α. It is not directly related to microstructural length scales [20, 47]. The idea of introducing more than one internal material length scale within the context of higher-order strain-gradient plasticity has been followed by several authors; see e.g., [1, 7, 11, 18, 26, 32, 36, 44].

2.2 Stress measures

Relevant stress measures are the first Piola–Kirchhoff stress

$$\boldsymbol{P} \;:=\; \det(\boldsymbol{F})\, \boldsymbol{\sigma} \cdot \boldsymbol{F}^{-t}, \tag{6}$$

and the elastic second Piola–Kirchhoff stress $\boldsymbol{S}_{\mathrm{e}}$ defined by

$$\boldsymbol{S}_{\mathrm{e}} := \det(\boldsymbol{F})\, {\boldsymbol{F}_{\mathrm{e}}}^{-1} \cdot \boldsymbol{\sigma} \cdot {\boldsymbol{F}_{\mathrm{e}}}^{-t} = [\boldsymbol{F}_{\mathrm{e}}]^{-1} \cdot \boldsymbol{P} \cdot [\boldsymbol{F}_{\mathrm{p}}]^{t} \,. \tag{7}$$

Whereas the Cauchy stress tensor $\boldsymbol{\sigma}$ is a stress measure in the current configuration $\mathcal{B}_t$, the second Piola–Kirchhoff stress $\boldsymbol{S}_{\mathrm{e}}$ is a stress measure in the intermediate configuration.

The resolved shear or Schmid stress τ_α is defined by

$$\tau_\alpha = \boldsymbol{s}_\alpha \cdot \boldsymbol{M}_{\mathrm{e}} \cdot \boldsymbol{n}_\alpha \tag{8}$$

where $\boldsymbol{M}_{\mathrm{e}} = \boldsymbol{C}_{\mathrm{e}} \cdot \boldsymbol{S}_{\mathrm{e}}$ is the Mandel stress.

2.3 Dislocation densities

During plastic deformation, two types of dislocations are present: statistically stored dislocations (SSDs) which are accumulated by a random trapping process and are responsible for plastic

deformation [3]; and geometrically necessary dislocations(GNDs) which arise due to the locally heterogeneous plastic shear. The first concepts of GNDs were introduced in [39] and [6] to account for modes of plastic deformation, where an internal accumulation of dislocation densities is required to accommodate the gradients of plastic strain induced by the deformation [35]. In this regard, GNDs are necessary to preserve lattice compatibility and represent an additional source of dislocations in the material due to inhomogeneous plastic flow [19]. In a continuum theory there are no discrete dislocations. However, non-uniform slips and slip gradients on the individual glide systems result in quantities that mimic the behavior of microscopic dislocations. The GNDs are usually subdivided into edge and screw dislocations, where edge dislocations are characterized by the fact that the Burgers vector is perpendicular to the dislocation line direction, while for screw dislocations the Burgers vector and one direction are parallel.

The simplest class of models for dislocation evolution is obtained for the case of self-interaction, in which the dislocations on each glide system interact only with themselves.

GNDs do not contribute to the plastic deformation: rather, they act as obstacles to the motion of the SSDs, leading to hardening in the material. The edge and screw dislocation densities are internal state variables defined by ([25], Sec. 107.4)

$$\dot{\rho}_\alpha^{\mathrm{ge}} = -\frac{1}{b}\nabla_{\boldsymbol{X}}\nu_\alpha \cdot \left[\boldsymbol{F}_{\mathrm{p}}^{-1}\cdot \boldsymbol{s}_\alpha\right] , \tag{9}$$

$$\dot{\rho}_\alpha^{\mathrm{gs}} = \frac{1}{b}\nabla_{\boldsymbol{X}}\nu_\alpha \cdot \left[\boldsymbol{F}_{\mathrm{p}}^{-1}\cdot \boldsymbol{p}_\alpha\right] , \tag{10}$$

where b is the magnitude of the Burgers vector. The initial conditions are assumed to be $\rho_\alpha^{\mathrm{ge}}(\boldsymbol{X},0)=0$ resp. $\rho_\alpha^{\mathrm{gs}}(\boldsymbol{X},0)=0$. The dislocation densities may be positive or negative.

Our definition of the GND density differs from that in [26] by the use of the length of the Burgers vector b. This is due to the fact that in [26] the theory is based strictly on continuum mechanics in which the GND is a quantity measured per unit length. In this work, we follow the approach generally used in material science where the GND represents a quantity measured in dislocations per unit area.

3 The mathematical model

3.1 Force balances

The macroscopic force balance equation is

$$\boldsymbol{0} = \mathrm{Div}\,\boldsymbol{P} + \boldsymbol{f}, \tag{11}$$

where $\boldsymbol{f}(\boldsymbol{x},t) : \mathcal{B}_0 \times \mathbb{R}_+ \to \mathbb{R}^{\mathrm{dim}}$ is the body force. Here and henceforth Div refers to the divergence with respect to the reference configuration, i.e., $\mathrm{Div}\{\bullet\} = \nabla_{\boldsymbol{X}} \cdot \{\bullet\}$

On the microlevel, we follow the approach in [21, 23] and introduce the microforce balance equation [1]

$$0 = \operatorname{Div} \boldsymbol{\xi}_{X,\alpha} + \tau_\alpha - \pi_\alpha, \tag{12}$$

where π_α is the scalar internal microforce and $\boldsymbol{\xi}_{X,\alpha}$ is the referential vector-valued microstress power-conjugate to the slip rate gradient $\nabla_{\boldsymbol{X}} \nu_\alpha$. The microforce balance (12) has to hold for every slip system α. The microstress $\boldsymbol{\xi}_{X,\alpha}$ is split into an elastic and a dissipative contribution, see e.g., [24]:

$$\boldsymbol{\xi}_{X,\alpha} = \boldsymbol{\xi}^{\text{en}}_{X,\alpha} + \boldsymbol{\xi}^{\text{dis}}_{X,\alpha}, \tag{13}$$

whereas the internal microforce π_α is purely dissipative in nature.

3.2 Boundary conditions

Associated with the momentum balance (11) is the traction condition

$$\boldsymbol{t}(\boldsymbol{N}) := \boldsymbol{P} \cdot \boldsymbol{N}, \tag{14}$$

where $\boldsymbol{t}$ denotes the macroscopic traction vector and $\boldsymbol{N}$ is the macroscopic outward unit vector. The traction vector $\boldsymbol{t}$ is prescribed on the boundary $\Gamma_{0,\boldsymbol{t}}$. On the complementary part $\Gamma_{0,\boldsymbol{u}}$ the displacement $\boldsymbol{u}$ is prescribed such that

$$\boldsymbol{u} := \bar{\boldsymbol{u}} \qquad \text{on } \Gamma_{0,\boldsymbol{u}}. \tag{15}$$

The microscopic boundary conditions are assumed to take the form

$$\begin{aligned} \nu_\alpha &= 0 \qquad \text{on } \Gamma_\nu\,, \\ \boldsymbol{\xi}_{X,\alpha} \cdot \boldsymbol{n} &= 0 \qquad \text{on } \Gamma_\xi\,, \end{aligned} \tag{16}$$

in which Γ_ν and Γ_ξ are complementary parts of the boundary Γ_0 in the reference configuration, with unit outward normal $\boldsymbol{n}$. The boundary condition on the slip rate is referred to as micro-hard, whereas that in terms of the microstress is called a micro-free boundary condition. The homogeneous boundary conditions correspond to the assumption of null expenditure of microscopic power on the boundary [24].

3.3 Dissipation inequality

The local dissipation inequality takes the form (see for example [25])

$$\dot{\psi} - \boldsymbol{S}_{\text{e}} : \dot{\boldsymbol{E}}_{\text{e}} - \sum_\alpha \left[\pi_\alpha \nu_\alpha + \boldsymbol{\xi}_{X,\alpha} \cdot \nabla_{\boldsymbol{X}} \nu_\alpha\right] \leq 0\,. \tag{17}$$

[1] The existence of the microforce balance (12) is a consequence of the principle of virtual power; cf. Gurtin [21] for a detailed derivation.

Now consider a free energy function of the form

$$\begin{aligned}\psi(\boldsymbol{E}_{\mathrm{e}}, \boldsymbol{\rho}^{\mathrm{ge}}) &= \psi_{\mathrm{e}}(\boldsymbol{E}_{\mathrm{e}}) + \psi_{\mathrm{gnd}}(\boldsymbol{\rho}^{\mathrm{ge}}) \\ &= \frac{1}{2}\boldsymbol{E}_{\mathrm{e}} : \boldsymbol{\mathcal{C}} : \boldsymbol{E}_{\mathrm{e}} + \frac{1}{2}b^2 \sum_{\alpha,\beta} h_{\mathrm{g0}}\, l_\alpha \left[\chi_{\alpha\,\beta} + \iota_{\alpha\,\beta}\right] l_\beta \rho_\alpha^{\mathrm{ge}} \rho_\beta^{\mathrm{ge}}\end{aligned} \tag{18}$$

with $\boldsymbol{\rho}^{\mathrm{ge}}$ being the set of edge GNDs, $\boldsymbol{\mathcal{C}}$ the fourth order elasticity tensor, l_α and l_β characteristic length scales and h_{g0} the gradient hardening modulus. $\chi_{\alpha\beta}$ are coplanarity moduli with

$$\chi_{\alpha\beta} = \begin{cases} 1 & \text{for } \alpha \text{ and } \beta \text{ coplanar,} \\ 0 & \text{for } \alpha \text{ and } \beta \text{ noncoplanar,} \end{cases} \tag{19}$$

see e.g., [4, 26, 29]. The interaction moduli $\iota_{\alpha\beta}$ are defined via

$$\iota_{\alpha\beta} = |\boldsymbol{s}_\alpha \cdot \boldsymbol{s}_\beta||\boldsymbol{n}_\alpha \times \boldsymbol{n}_\beta|, \tag{20}$$

as suggested by Nix[2]. A similar form $(\boldsymbol{s}_\alpha \cdot \boldsymbol{s}_\beta)$ has been used by [22, 34, 12, 9]. For coplanar slip systems as well as for $\boldsymbol{s}_\alpha$ and $\boldsymbol{s}_\beta$ being orthogonal, the interaction moduli vanish. As a consequence, if the Burgers vectors of colliding dislocations are orthogonal, the modeled interaction between those glide systems is small, see e.g., [13].

Substitution in the free energy inequality leads, after the usual arguments, to the elastic law

$$\boldsymbol{S}_{\mathrm{e}} = \boldsymbol{\mathcal{C}} : \boldsymbol{E}_{\mathrm{e}}, \tag{21}$$

which we assume to model a St. Venant type material. Defining the referential energetic microstress $\boldsymbol{\xi}_{X,\alpha}^{\mathrm{en}}$ by

$$\boldsymbol{\xi}_{X,\alpha}^{\mathrm{en}} = -\frac{1}{b}\frac{\partial \psi_{\mathrm{gnd}}}{\partial \rho_\alpha}\left[\boldsymbol{F}_p^{-1} \cdot \boldsymbol{s}_\alpha\right], \tag{22}$$

we obtain the reduced dissipation inequality

$$\sum_\alpha \left[\pi_\alpha \nu_\alpha + \boldsymbol{\xi}_{X,\alpha}^{\mathrm{dis}} \cdot \nabla_{\boldsymbol{X}} \nu_\alpha\right] \geq 0 \tag{23}$$

or, in compact form,

$$\boldsymbol{\Sigma}_\alpha^{\mathrm{dis}} : \boldsymbol{\Gamma}_\alpha \geq 0, \tag{24}$$

where the inner product $\boldsymbol{\Sigma}_\alpha^{\mathrm{dis}} : \boldsymbol{\Gamma}_\alpha$ is to be understood componentwise and the dissipative generalized stress $\boldsymbol{\Sigma}_\alpha^{\mathrm{dis}}$ is defined by

$$\boldsymbol{\Sigma}_\alpha^{\mathrm{dis}} = \begin{pmatrix} \pi_\alpha \\ l_{d,\alpha}^{-1} \boldsymbol{\xi}_{X,\alpha}^{\mathrm{dis}} \end{pmatrix}. \tag{25}$$

[2] in a private communication with Gurtin, see also [26]

4 Description of plastic behavior

In the literature, there exists a variety of descriptions of hardening behavior for single crystals. We focus here on a relation introduced by Gurtin and Reddy [26], which accounts for both self- and latent-hardening as a function of the accumulated generalized slips $\Gamma_{\mathrm{acc},\alpha}$, defined here for the large-deformation case by

$$\Gamma_{\mathrm{acc},\alpha} := \int_t d_\alpha \, \mathrm{d}t \,,$$

in which

$$d_\alpha := |\boldsymbol{\Gamma}_\alpha| = \sqrt{|\nu_\alpha|^2 + l_{d,\alpha}^2 |\nabla_{\boldsymbol{X}} \nu_\alpha|^2}$$

is the magnitude of the generalized slip rate.

We make use of the form of the hardening relation in which the dependence on $\Gamma_{\mathrm{acc},\alpha}$ is linear, and is given by

$$S_\alpha = S_0 + S_{\mathrm{slf}} \sum_\beta \chi_{\alpha\beta} \Gamma_{\mathrm{acc},\beta} + S_{\mathrm{lat}} \sum_\beta \iota_{\alpha\beta} \Gamma_{\mathrm{acc},\beta} \,. \tag{26}$$

Here, $\chi_{\alpha\beta}$ and $\iota_{\alpha\beta}$ are the moduli defined by Eqs. (19) and (20), and S_{slf} and S_{lat} are constants. The hardening relation (26) is calibrated in [26] against that of Anand and Kothari [2] for the conventional (non-gradient) theory; when extended to the gradient case it is shown to take the form

$$S_\alpha = S_0 + [S_s - S_0] \left[1 - \frac{1}{1 + \frac{S_s - S_0}{S_s} \frac{h_0}{S_s} \sum_\beta \chi_{\alpha\beta} \Gamma_{\mathrm{acc},\beta}} \right] + q \, [S_s - S_0] \left[1 - \frac{1}{1 + \frac{S_s - S_0}{S_s} \frac{h_0}{S_s} \sum_\beta \iota_{\alpha\beta} \Gamma_{\mathrm{acc},\beta}} \right] . \tag{27}$$

The parameter $q > 0$ is the ratio of latent-hardening to self-hardening and stipulates the degree of interaction of the slip systems, h_0 is the initial hardening rate of each system, $S_\alpha|_{t=0} = S_0$ the initial slip resistance and S_s the saturation value of S.

4.1 The standard crystal plasticity theory without gradient effects

For the standard crystal plasticity theory the yield function is defined on the αth slip system by

$$\Phi_\alpha(\pi_\alpha, S_\alpha) = \left[\frac{|\pi_\alpha|}{S_\alpha} \right]^{\frac{1+m_0}{m_0}} - 1 \leq 0 \,. \tag{28}$$

The set of yield functions defines a convex elastic region $\mathbb{E} := \{(\pi_\alpha, S_\alpha) |\ \Phi_\alpha(\pi_\alpha, S_\alpha) < 0\}$. Its boundary $\{(\pi_\alpha, S_\alpha) | \Phi_\alpha = 0\}$ is the yield surface. The flow relation is assumed to be of the associative type and the yield surface smooth, so that

$$\nu_\alpha = \lambda_\alpha \frac{\partial \Phi_\alpha}{\partial \pi_\alpha}, \tag{29}$$

in which λ_α is the set of Lagrange multipliers. This equation must be supplemented by the complementarity conditions

$$\lambda_\alpha \geq 0, \quad \Phi_\alpha \leq 0, \quad \lambda_\alpha \Phi_\alpha = 0\,. \tag{30}$$

From (29) the scalar multipliers are given by

$$\lambda_\alpha = S_\alpha \frac{m_0}{1+m_0} |\nu_\alpha|. \tag{31}$$

Substitution of Eq. (31) in Eq. (29) then gives

$$\nu_\alpha = |\nu_\alpha| \left[\frac{|\pi_\alpha|}{S_\alpha}\right]^{\frac{1}{m_0}} \operatorname{sign}(\pi_\alpha). \tag{32}$$

We are aiming at a rate-dependent theory, which is obtained as a regularization of the rate-independent theory. Here, we choose a viscoplastic approximation for the regularization and add a penalty term of the Norton–Hoff type [38] to the reduced dissipation inequality (23). In order to obtain the rate-dependent counterpart of (32), the resulting Lagrangian is minimized, yielding

$$\nu_\alpha = \frac{1}{t_{\star,\alpha}} \left[\frac{|\pi_\alpha|}{S_\alpha}\right]^{\frac{1}{m_0}} \operatorname{sign}(\pi_\alpha), \tag{33}$$

where $t_{\star,\alpha}$ is the relaxation time. Within a standard crystal plasticity framework, the microscopic stresses $\boldsymbol{\xi}_\alpha$ vanish. Thus, the microforce balance (12) reduces to

$$\tau_\alpha = \pi_\alpha. \tag{34}$$

Moreover, the relation for the slip resistance S_α given in Eq. (27) simplifies to

$$\begin{aligned} S_\alpha \;=\; & S_0 + [S_s - S_0] \left[1 - \frac{1}{1 + \frac{S_s - S_0}{S_s} \frac{h_0}{S_s} \sum_\beta \chi_{\alpha\beta} \int_{t_0}^t |\nu_\beta| \mathrm{d}t}\right] \\ & + q\,[S_s - S_0] \left[1 - \frac{1}{1 + \frac{S_s - S_0}{S_s} \frac{h_0}{S_s} \sum_\beta \iota_{\alpha\beta} \int_{t_0}^t |\nu_\beta| \mathrm{d}t}\right]. \end{aligned} \tag{35}$$

4.2 Gradient extended crystal plasticity theory: energetic theory

In this Section, we extend our analysis to gradient extended crystal plasticity. It is assumed that the microstress is entirely energetic in nature, i.e.

$$\boldsymbol{\xi}_{X,\alpha} = \boldsymbol{\xi}^{\mathrm{en}}_{X,\alpha}.$$

Consequently, the second term on the left-hand side of Eq. (23) vanishes and the reduced dissipation inequality reads

$$\sum_\alpha \pi_\alpha \nu_\alpha \geq 0\,. \tag{36}$$

Via the microforce balance (12) the microforce π_α is given by

$$\pi_\alpha = \tau_\alpha + \operatorname{Div} \boldsymbol{\xi}^{\mathrm{en}}_{X,\alpha} \tag{37}$$

and can be inserted into Eq. (33). This leads to a flow rule in which the plastic slip rate ν_α (via τ_α) depends on the slip rate itself as well as the slip rate gradient $\nabla_{\boldsymbol{X}}\nu_\alpha$ (via $\rho^{\mathrm{ge}}_\alpha$)

$$\nu_\alpha = \frac{1}{t_{\star,\alpha}} \left[\frac{\left| \tau_\alpha + \operatorname{Div}\left(-b \sum_{\alpha,\beta} h_{\mathrm{g}0}\, l_\alpha \left[\chi_{\alpha\beta} + \iota_{\alpha\beta}\right] l_\beta \rho^{\mathrm{ge}}_\beta \boldsymbol{F}_p^{-1} \cdot \boldsymbol{s}_\alpha \right) \right|}{S_\alpha} \right]^{\frac{1}{m_0}} \operatorname{sign}(\pi_\alpha). \tag{38}$$

The glide system interaction in the material's hardening behavior is modeled via relation (35). Thus, although the flow rule is gradient-dependent, the slip resistance is not (since for this case the dissipative length scale vanishes $l_{d,\alpha}$).

4.3 The full gradient theory

The theory discussed in this Section includes, in addition to energetic hardening driven by the slip gradient, dissipative hardening associated with plastic strain rate gradients.

The starting point for a theory based on an associative flow relation is the reduced dissipation inequality (24): following [43, 44, 45], but here generalized to the rate-dependent case, we define the yield function Φ by

$$\Phi_\alpha(\boldsymbol{\Sigma}^{\mathrm{dis}}_\alpha, S_\alpha) = \left[\frac{|\boldsymbol{\Sigma}^{\mathrm{dis}}_\alpha|}{S_\alpha} \right]^{\frac{1+m_0}{m_0}} - 1 \leq 0. \tag{39}$$

The rate-independent flow law now reads

$$\boldsymbol{\Gamma}_\alpha = \lambda^{\mathrm{dis}}_\alpha \frac{\partial \Phi_\alpha}{\partial \boldsymbol{\Sigma}^{\mathrm{dis}}_\alpha}, \tag{40}$$

together with the the complementarity conditions $\lambda^{\mathrm{dis}}_\alpha \geq 0, \quad \Phi_\alpha \leq 0, \quad \lambda^{\mathrm{dis}}_\alpha \Phi_\alpha = 0$. Following the same procedure as that leading to Eq. (33), the generalized, rate-dependent counterpart of Eq. (33) yields

$$\boldsymbol{\Gamma}_\alpha = \frac{1}{t_{\star,\alpha}} \left[\frac{|\boldsymbol{\Sigma}^{\mathrm{dis}}_\alpha|}{S_\alpha} \right]^{\frac{1}{m_0}} \frac{\boldsymbol{\Sigma}^{\mathrm{dis}}_\alpha}{|\boldsymbol{\Sigma}^{\mathrm{dis}}_\alpha|}. \tag{41}$$

Evaluation componentwise of the generalized flow rule (41) yields

$$\begin{aligned} \nu_\alpha &= \frac{1}{t_{\star,\alpha}} \left[\frac{|\boldsymbol{\Sigma}^{\mathrm{dis}}_\alpha|}{S_\alpha} \right]^{\frac{1}{m_0}} \frac{\tau_\alpha + \operatorname{Div} \boldsymbol{\xi}_{X,\alpha}}{|\boldsymbol{\Sigma}^{\mathrm{dis}}_\alpha|}, \\ l^2_{d,\alpha} \nabla_{\boldsymbol{X}} \nu_\alpha &= \frac{1}{t_{\star,\alpha}} \left[\frac{|\boldsymbol{\Sigma}^{\mathrm{dis}}_\alpha|}{S_\alpha} \right]^{\frac{1}{m_0}} \frac{\boldsymbol{\xi}^{\mathrm{dis}}_{X,\alpha}}{|\boldsymbol{\Sigma}^{\mathrm{dis}}_\alpha|}, \end{aligned} \tag{42}$$

with $|\boldsymbol{\Sigma}_\alpha^{\mathrm{dis}}| = \sqrt{\left[\tau_\alpha + \mathrm{Div}\left(\boldsymbol{\xi}_{X,\alpha}^{\mathrm{en}} + \boldsymbol{\xi}_{X,\alpha}^{\mathrm{dis}}\right)\right]^2 + l_{d,\alpha}^{-2}\boldsymbol{\xi}_{X,\alpha}^{\mathrm{dis}} \cdot \boldsymbol{\xi}_{X,\alpha}^{\mathrm{dis}}}$. The glide system resistance S_α is obtained from (35).

5 Numerical results

The following numerical examples elucidate the theory presented in the previous sections. We restrict our analysis to two-dimensional plane strain problems with glide systems lying in the plane of deformation. Thus, the transverse direction $\boldsymbol{p}_\alpha$ is perpendicular to the plane, resulting in no screw GNDs. Further, $\boldsymbol{s}_\alpha$ and $\boldsymbol{n}_\alpha$ are assumed to be equal to the corresponding vectors in the undeformed configuration (isoclinic assumption). Single as well as polycrystals are investigated. The material properties of the simulations are listed in Table 1. Our main goal is the discussion of the hardening behavior of the material under the different hardening descriptions.

Parameter	Symbol	Value	
Young's modulus	E	210	[GPa]
Poisson's ratio	ν	0.3	
relaxation time	$t_{\star,\alpha}$	1000	[s]
rate sensitivity parameter	m_0	1	
Burgers vector magnitude	b	0.256	[nm]
characteristic length	l_α	0.1	[mm]
gradient hardening modulus	$h_{\mathrm{g}0}$	$1.5 \cdot 10^4$	[MPa]
initial hardening rate	h_0	180	[MPa]
initial slip resistance	S_0	16	[MPa]
saturation of slip resistance	S_s	148	[MPa]
ratio of latent-hardening to self-hardening	q	1.4	
dissipative length scale	l_d	0.05	[mm]

Table 1: Material parameter values for soft metals adopted for the mathematical model: h_0, S_0, S_s are chosen as in [2]. q is given as in [5, 40]. The chosen value for the gradient hardening modulus $h_{\mathrm{g}0}$ is in accordance with values suggested by other authors: for example, in [17] it is given in terms of Young's modulus E and Poisson's ratio ν by $E/[16\,[1-\nu^2]]$, resulting in a similar value. For the current model formulation of the free energy density (18), the ratio of characteristic sample size, i.e. smallest edge length, to characteristic material length l_α is of importance but not their absolute values. In the current work the choice $m_0 = 1$ is made for simplicity, analogous to discrete dislocation modeling based on linear drag, for example.

In the current work, the numerical implementation is based on a dual-mixed finite element formulation (see e.g., [10, 16]), in which the gradient of the plastic slip rate is treated as a global variable, while the plastic slip rate is solved for locally.

The dual-mixed formulation imposes the micro-hard slip boundary conditions only in a weak sense. Furthermore, the plastic slip rate is only zero in the normal direction at the boundary.

We explicitly account for micro-hard boundary conditions with boundary elements of finite thickness which have the advantage at mimicking different types of boundary conditions, e.g., grain boundaries partially transparent to dislocations based on the misorientation between the grains (see for example [15, 9]).

In the following, the results are presented in terms of the accumulated generalized slip

$$\Gamma_{\mathrm{acc},\alpha\, n+1} = \Gamma_{\mathrm{acc},\alpha\, n} + \Delta t_{n+1} \sqrt{\sum_{\alpha} \left[\nu_{\alpha\, n+1}^2 + |l_{d,\alpha} \nabla_{\boldsymbol{X}} \nu_{\alpha\, n+1}|^2\right]}, \tag{43}$$

and the effective GND

$$\rho_{\mathrm{eff}\, n+1} = \sqrt{\sum_{\alpha} \rho_{\alpha\, n+1}^2}. \tag{44}$$

We present results showing the response of the material for the gradient theory with only energetic microstresses, and for the full gradient theory, that is, with both energetic and dissipative microstresses.

5.1 Single crystal, single slip

First, we have a look at the hardening behavior for the case of single slip (with orientation $\varphi = 15^\circ$ with respect to the x-axis). The benchmark problem of simple shear of a square single crystal with side length $l_0 = 1.1\mathrm{mm}$ is considered. The imposed macroscopic shear rate $\dot{\varepsilon}$ is $0.01\ \mathrm{s}^{-1}$. During the observation time of 50 s, two full loading and one full unloading cycles are run. In the finite element mesh, a boundary layer with a thickness of 0.05 mm is introduced (see Fig. 1). The mechanical boundary conditions read $\boldsymbol{u}([x, 0], t) = \boldsymbol{0}$ and $\boldsymbol{u}([x, 1.1\mathrm{mm}], \mathrm{t}) = [1.1\mathrm{mm} \times \varepsilon(\dot{\varepsilon}, \mathrm{t}), 0]$, where

$$\varepsilon(\dot{\varepsilon}, t) = \dot{\varepsilon} \times \begin{cases} t & , \quad 0\mathrm{s} \leq \mathrm{t} < 10\mathrm{s}, \\ 20\mathrm{s} - \mathrm{t} & , \quad 10\mathrm{s} \leq \mathrm{t} < 30\mathrm{s}, \\ -40\mathrm{s} + \mathrm{t} & , \quad 30\mathrm{s} \leq \mathrm{t} < 50\mathrm{s}, \end{cases}$$

as depicted in Fig. 1 and $\nu_\alpha(\boldsymbol{X} \in \text{boundary elements}) = 0$ in the boundary elements for all slip systems α. The remaining boundary conditions read $\boldsymbol{t}([0, y], t) = \boldsymbol{0}$ and $\boldsymbol{t}([1.1\mathrm{mm}, \mathrm{y}], \mathrm{t}) = 0$. The initial conditions are $\boldsymbol{u}(\boldsymbol{X}, 0) = \boldsymbol{0}$ and $\nu_\alpha(\boldsymbol{X}, 0) = 0$ for all α and all $\boldsymbol{X}$.

In Fig. 2 the results for the plastic slip Γ_{acc} are shown for the gradient theory in which the microstress is modeled as purely energetic. A gradual plastic slip distribution develops within

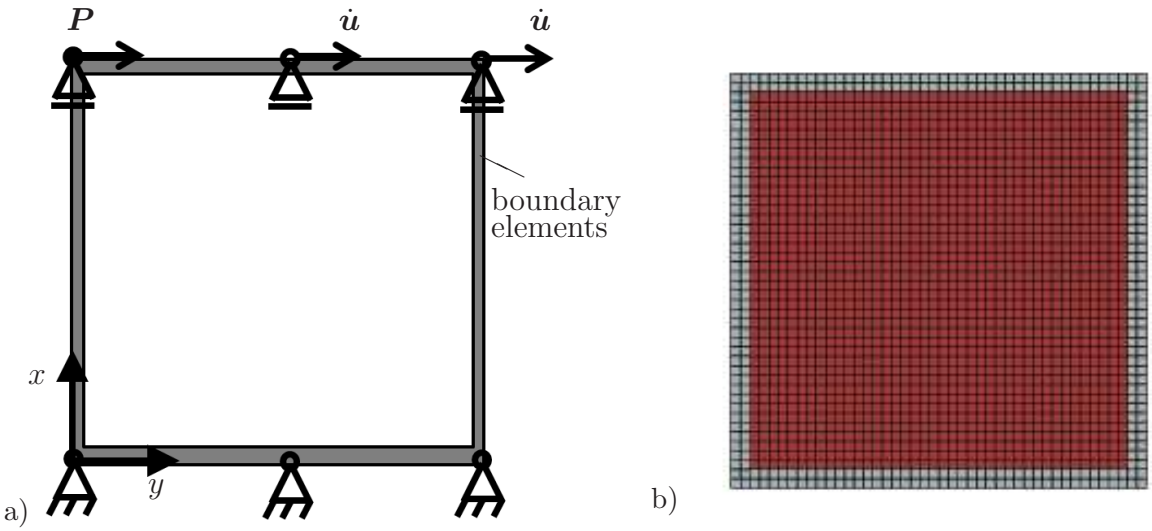

Figure 1: a) Sketch of single crystal. Size $l_0 \times l_0$ of edge length $l_0 = 1.1$ mm. Boundary elements are introduced. The applied boundary conditions are indicated as well. b) FE discretization of single crystal. The thickness of the boundary layer is chosen to be 0.05 mm.

the crystal with a rather smooth maximum in the middle. The shape of the plastic deformation distribution is mainly determined by the glide system orientation $\varphi = 15°$. As is usually observed in gradient plasticity, the plastic slip decreases gradually to the boundary. The corresponding distribution of the geometrically necessary dislocations is shown in Fig. 3. Clearly, strong dislocation pile-up at the boundary is visible. The maximum is reached at the transition between bulk material and boundary element.

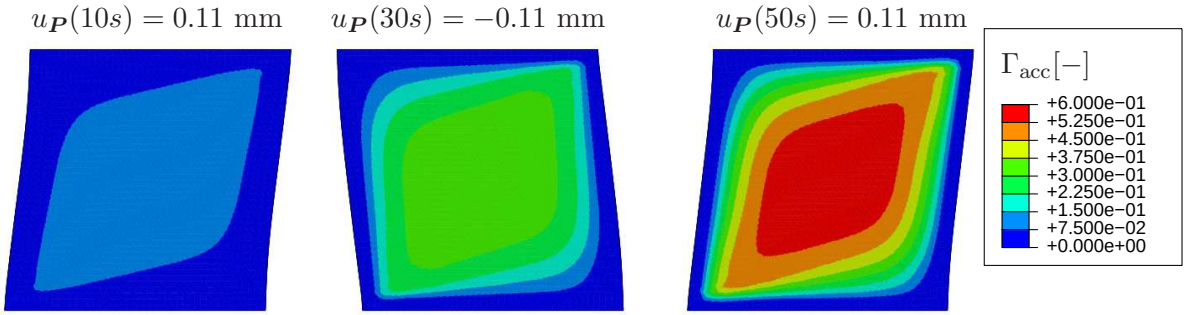

Figure 2: Energetic gradient crystal plasticity theory: Γ_{acc}-distribution in a single crystal for single slip at three deformation states (denoted by displacement at point $\boldsymbol{P}$: $u_{\boldsymbol{P}}$). The plastic slip distribution gradually decreases to the boundary due to the fact that micro-clamped slip boundary conditions are assumed.

Fig. 4 shows the average stress-strain behavior.Local hardening is visible for the standard crystal plasticity theory. The load reversal indicates that hardening as well as rate effects are purely

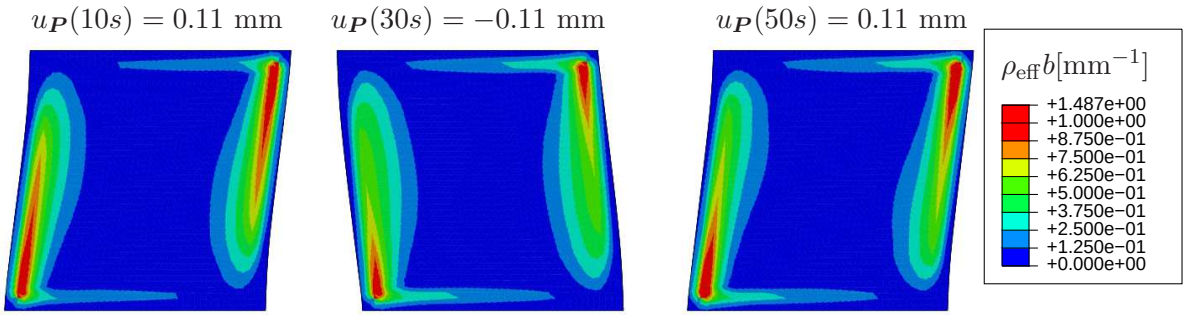

Figure 3: Energetic gradient crystal plasticity theory: ρ_{eff}-distribution in a single crystal for single slip at three deformation states (denoted by displacement at point $\boldsymbol{P}$: $u_{\boldsymbol{P}}$). The dislocation distribution decreases after the transition due to the fact that within the boundary elements no plastic slip is present.

isotropic. Although a simplified form of local hardening is implemented, the slope indicates saturation behavior as intended.

In contrast to the standard crystal plasticity theory, the hardening is significantly higher for the gradient case. Considering the microstress as purely energetic, the resolved shear stress increases with an almost-linear slope behind the elastic region. The change in the loading direction clearly reveals that a large amount of the hardening is kinematic, capturing the well known Bauschinger effect. Fig. 5 displays the average local hardening behavior S_α vs. the average effective plastic slip Γ_{acc}. The local hardening of the energetic theory is slightly lower than in the standard crystal plasticity theory - which might be a result of the difference in the plastic slip distribution having an effect on the plastic slip rate behavior.

Next, we turn to the full gradient crystal plasticity theory, that is, including the dissipative microstress. This results in a change of the plastic slip distribution near the boundary where the geometrically necessary dislocations are accumulated. Contrary to expectations, regions of higher generalized plastic slip develop near these boundaries, see Fig. 6 (especially in top right and bottom left corner). However, this is a result of the definition of the generalized plastic slip Γ_{acc}, accounting for the plastic slip as well as the gradient of it multiplied by the plastic length scale l_{d}. The GND distribution ρ_{eff}, shown in Fig. 7, is similar to that for the energetic theory with a lower maximum value. This indicates that the dissipative microstress mainly influences the plastic slip distribution but has no significant influence on the GND distribution. The stress-strain behavior in Fig. 4 shows an additional strengthening effect, occurring directly at the beginning of yielding, which leads to an initial kinematic hardening contribution. However, due to the definition of the generalized plastic slip based on the dissipative length scale l_{d} an effect in the local hardening behavior is observed in Fig. 5 as well.

A central difference between the three theories is the resulting macroscopic stress-strain behavior.

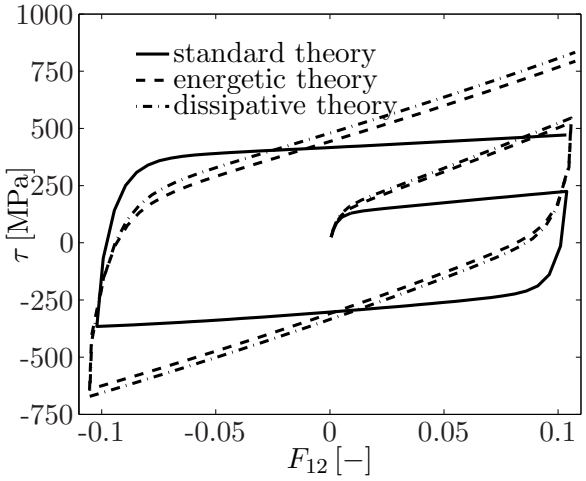

Figure 4: Single crystal, single slip. Macroscopic deformation F_{12} vs. average resolved shear stress τ for the standard crystal plasticity theory, energetic and dissipative gradient crystal plasticity theory.

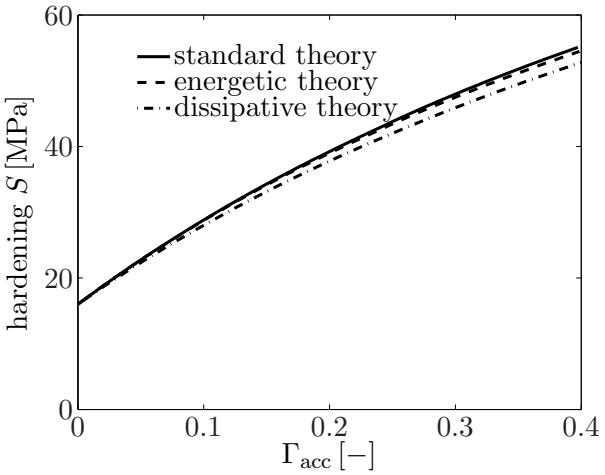

Figure 5: Single crystal, single slip. Local hardening development S_α vs. average effective plastic slip Γ_{acc} for the standard crystal plasticity theory (no gradient effects), energetic and dissipative gradient crystal plasticity theory.

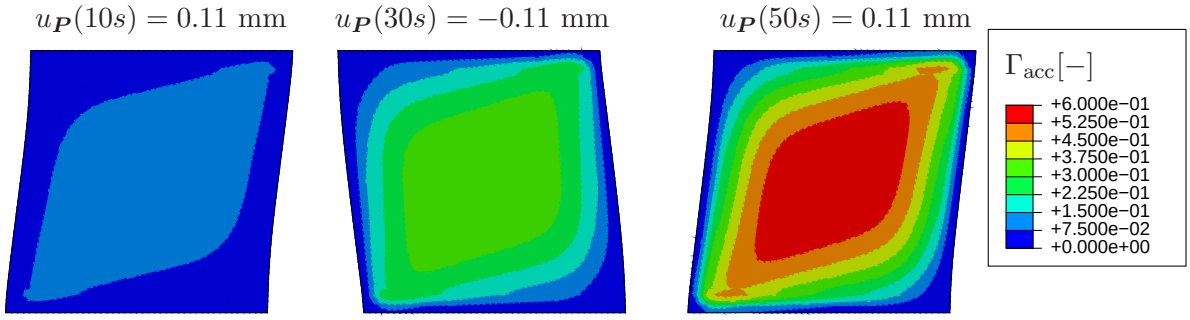

Figure 6: Dissipative gradient crystal plasticity theory: Γ_{acc}-distribution in a single crystal with one active slip system at three deformation states (denoted by displacement at point $\boldsymbol{P}$: $u_{\boldsymbol{P}}$).

Including an energetic microstress leads to kinematic hardening and an additional dissipative microstress results in a strengthening effect of the material.

5.2 Single crystal, multiple slip

In this Section we consider the same single crystal, but with multiple active slip systems. Both self- and latent-hardening take place.

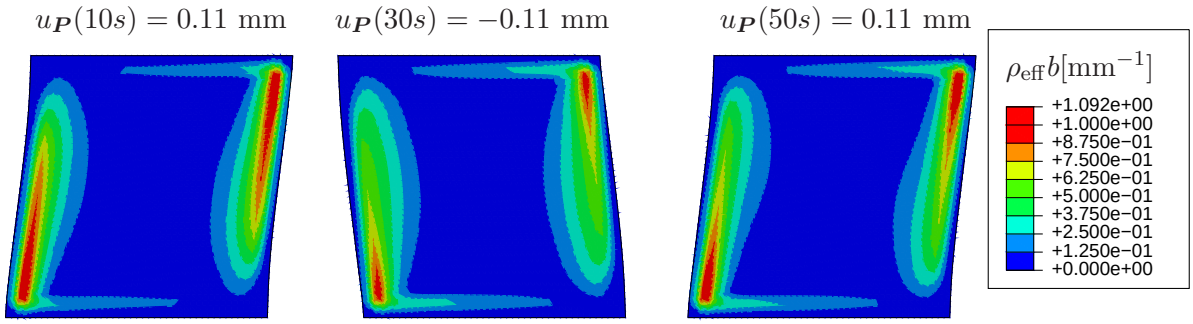

Figure 7: Dissipative gradient crystal plasticity theory: ρ_{eff}-distribution in a single crystal with one active slip system at three deformation states (denoted by displacement at point $\boldsymbol{P}$: $u_{\boldsymbol{P}}$).

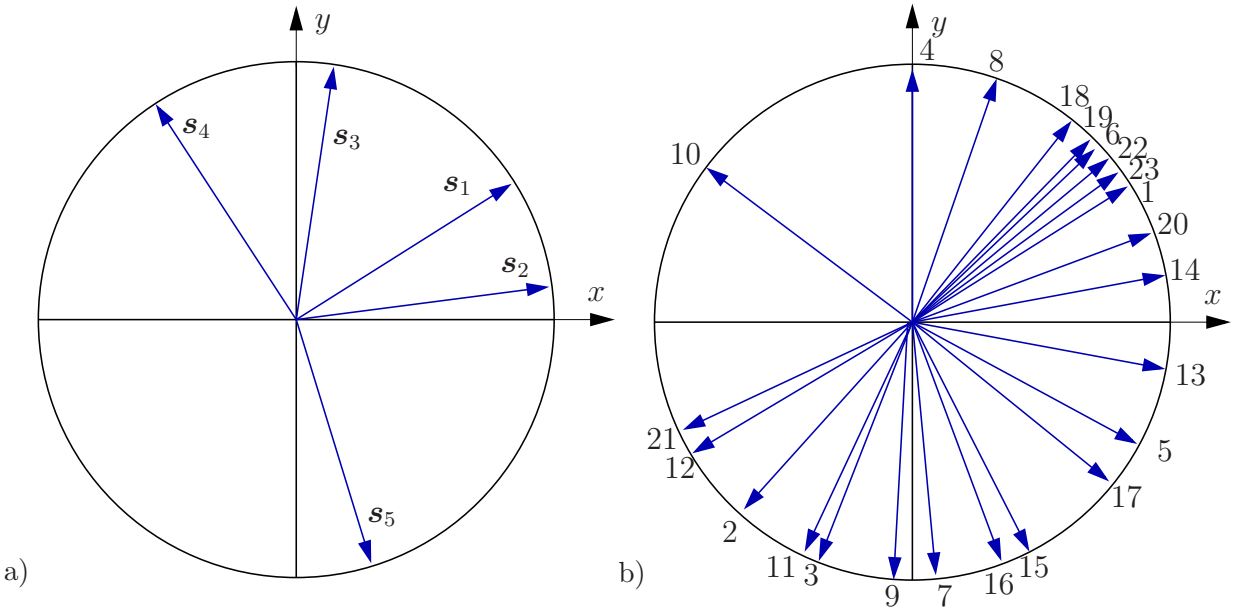

Figure 8: a) Single crystal: Slip system directions $\boldsymbol{s}_1 - \boldsymbol{s}_5$. b) Polycrystal: Direction of slip system direction $\boldsymbol{s}_1$ for the 23 grains; Each grain has five active slip systems which are oriented relative to each other as in the single crystal case a).

Five slip systems with random orientation are considered, see Fig. 8(a). Since conventional single-crystal plasticity is well documented in the literature we focus on the energetic and the full gradient theories. Fig. 9 (left) displays the resulting generalized slip Γ_{acc} distribution for the energetic gradient crystal plasticity theory, including self- and latent hardening. A region of high plastic slip is observed in the middle of the crystal. The plastic slip decreases towards the boundaries due to the applied micro-hard boundary conditions. Simulation results for the energetic gradient theory, with self-hardening only, show a very similar distribution of Γ_{acc}. This

indicates that the effect of latent hardening on the shape of the plastic slip distribution (not its magnitude) is relatively small.

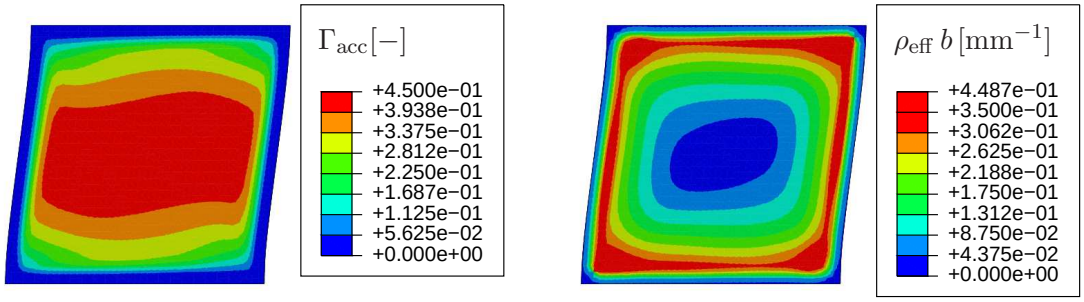

Figure 9: Energetic gradient crystal plasticity theory. Left: Γ_{acc}-distribution at $u_{\boldsymbol{P}}(50s) = 0.11$ mm.
Right: $\rho_{\text{eff}} = \sqrt{\sum_\alpha \varrho_\alpha^2}$-distribution at $u_{\boldsymbol{P}}(50s) = 0.11$ mm.

The analysis of the different slip systems shows that the glide systems are loaded very differently. In our example, glide system $\alpha = 1$ experiences the lowest stress; glide system $\alpha = 3$ shows the highest resolved shear stress and $\tau_1 \leq \tau_4 \leq \tau_5 \leq \tau_2 \leq \tau_3$ holds. Fig. 10 displays the average resolved shear stress distribution τ_α for glide systems 1, 3, and 5.

To investigate the effect of latent hardening on the material response, the results for the energetic gradient crystal plasticity theory including only self-hardening are also shown in Fig. 10. Clearly, for the case of self-hardening the resolved shear stress on each glide system is lower than for latent hardening. As a consequence, the macroscopic stress is lower if only self-hardening is considered, see Fig. 12. The general stress-strain behavior is similar in both models, e.g., the initial yield point is the same as well as the shape of the stress-strain curves. However, the stress level is significantly higher for the model including latent hardening. To quantify this effect in greater detail, Fig. 11 presents the average local hardening behavior for three exemplar glide systems. The average local hardening on glide system $\alpha = 3$ is higher than that for the other glide systems for both cases. The non-diagonal terms of the matrix $\iota_{\alpha\,\beta}$, representing the interaction between the different glide systems, is different for each interaction, with a maximum value 0.5. Considering that $q = 1.4$, effective 0.7 is the ratio between latent and self hardening between two glide systems. On glide system $\alpha = 3$, self-hardening is stronger than the sum of the latent hardening. In contrast, glide system $\alpha = 5$ shows a local hardening behavior similar to the glide system $\alpha = 1$, although self hardening is much stronger on glide system $\alpha = 5$.

For the purely energetic theory with self-hardening accounted for, the scaling of the hardening on the different glide systems is in accordance to the level of activity. Glide system $\alpha = 3$ hardens most and glide system $\alpha = 1$ experiences negligible hardening. In addition to local latent hardening, latent hardening due to GNDs (latent gradient hardening) influences the stress level as well.

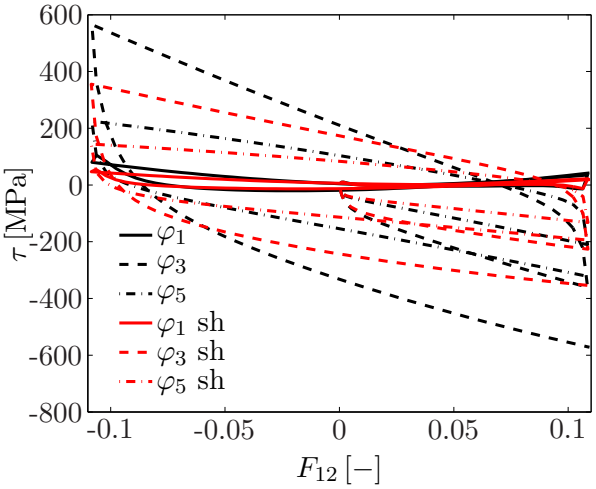

Figure 10: Energetic gradient crystal plasticity theory: Comparison of average local resolved shear stress τ over average deformation F_{12} between model including self and latent hardening and the model including only self hardening (sh) for three exemplar glide systems. For the glide systems 3 and 5, the typical stress-strain curves including isotropic and kinematic hardening are observed.

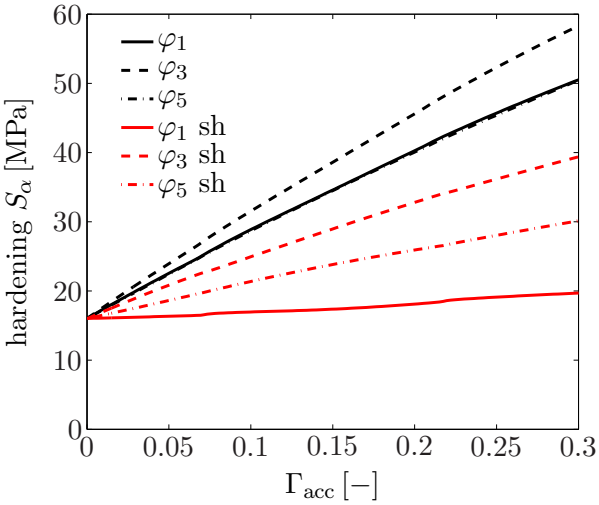

Figure 11: Energetic gradient crystal plasticity theory: Comparison of average local hardening S_α over average effective plastic slip Γ_{acc} between model including self and latent hardening and the model including only self hardening (sh) for three exemplary glide systems.

Next, the effective general plastic slip Γ_{acc} distribution is shown in Fig. 14 (left) for the full gradient theory. As in the single slip case, the distribution differs from the results of the energetic theory near the boundary. As stated above, this results from the definition of the general plastic slip Γ_{acc} which includes the gradient of the plastic slips as well. Here, boundary layer at all boundaries are visible. Fig. 14 (right) represents the corresponding effective dislocation ρ_{eff} distribution obtained with the full theory, which is very similar to that obtained for the energetic theory. The dissipative microstress leads to a dissipative strengthening characterized by an increase in the yield stress. This effect increases with each load change. Due to the coupling between the dissipative microstress to the current local hardening, an additional strengthening on each glide system with one-going deformation apart from each load change is observed as well, see Fig. 13, as well as in the macroscopic behavior (see Fig. 12): If local hardening increases, the microstress increases as well, leading to additional strengthening in the material. This effect is stronger for multiple slip compared to single slip where this effect can be anticipated, but is not clearly recognizable.

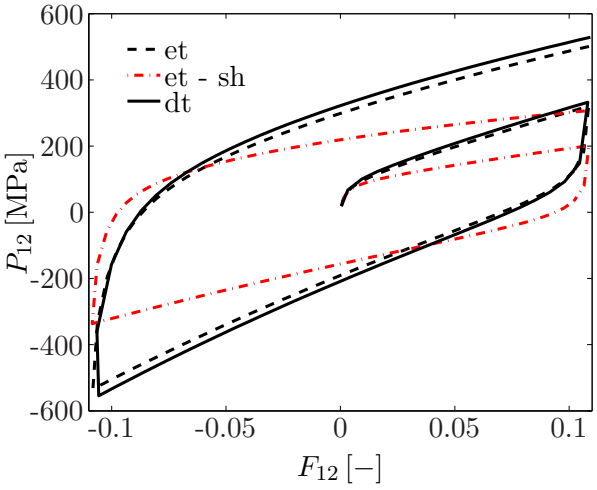

Figure 12: Single crystal, multiple slip: Comparison of macroscopic stress-strain behavior between energetic gradient crystal plasticity theory including self and latent hardening (et), energetic gradient crystal plasticity theory considering only self hardening (et-sh) and dissipative gradient theory (dt).

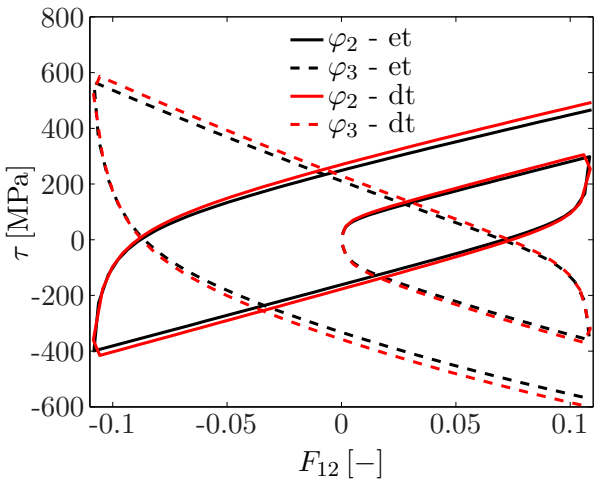

Figure 13: Single crystal, multiple slip: Local comparison of resolved shear stress τ over deformation F_{12} between energetic gradient theory including self and latent hardening (et) and dissipative gradient theory (dt) for two exemplary slip systems.

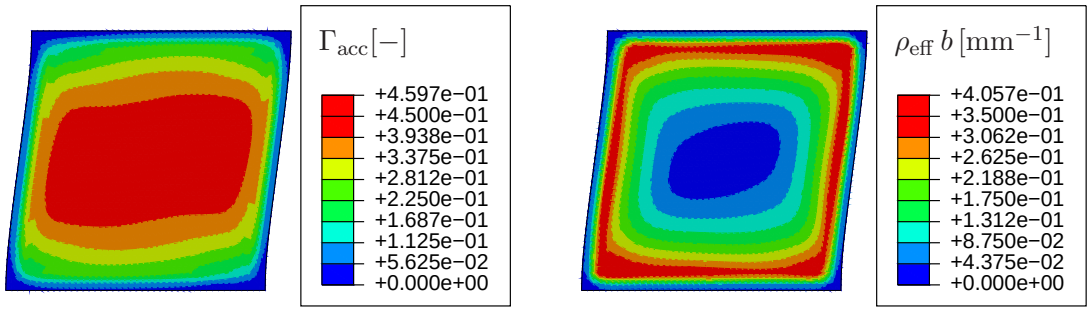

Figure 14: Dissipative gradient crystal plasticity theory:. Left: Γ_{acc}-distribution at $u_{\boldsymbol{P}}(50s) = 0.11$ mm.
Right: $\rho_{\text{eff}} = \sqrt{\sum_\alpha \varrho_\alpha^2}$-distribution at $u_{\boldsymbol{P}}(50s) = 0.11$ mm.

5.3 Oligocrystal, multiple slip

The oligocrystal displayed in Fig. 15 is considered next (see [28] for an experimental characterization and [30] for a numerical investigation). The orientation for each grain is given in Fig.

8b)[3]. Each grain has five active glide systems which are oriented relative to each other as in the single crystal case (cf. Fig. 8a)). As previously, finite boundary elements of a thickness 0.05 mm are introduced at each grain boundary. We apply tensile loading with a rate $\dot{\varepsilon} = 0.01s^{-1}$ at the right boundary. The left boundary is fixed. The two outer grains (i.e., the left and the right grain) are modeled as elastic to act as a transmission zone.

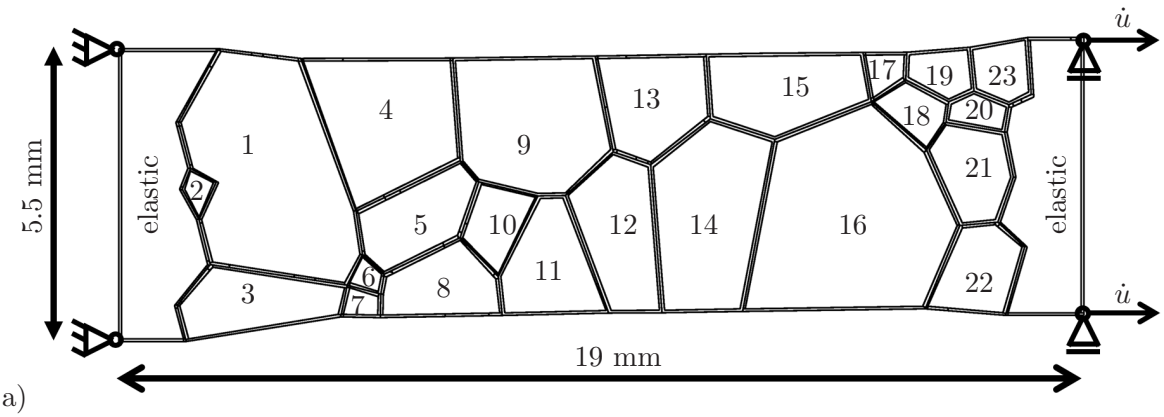

a)

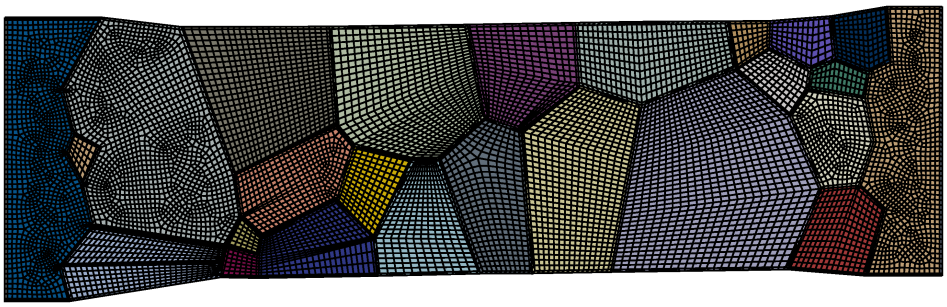

b)

Figure 15: a) Oligocrystal consisting of 25 different grains. b) FE discretization: approx. 12000 quad elements.

Fig. 16 shows the effective plastic slip Γ_{acc} distribution and in Fig. 17 the effective dislocation density ρ_{eff} distributions displayed at $F_{11} = 1.1$ for the different theories. With the standard crystal plasticity theory, significant deformation at the top boundary takes place, in particular between grains 1 and 3; this may be associated with a type of necking behavior. At this grain boundary, a strong jump in the plastic deformation is visible. Due to the fact that a continuous strain transition between the grains over the grain boundaries is satisfied, the large difference indicates that grain 1 is more favorable to the applied deformation than grain 3. Such examples are found at several positions within the sample. For the energetic gradient theory, the micro-

[3]Due to restriction to two dimension and five glide systems, the orientations are artificial chosen and do not represent the experimental measured orientations.

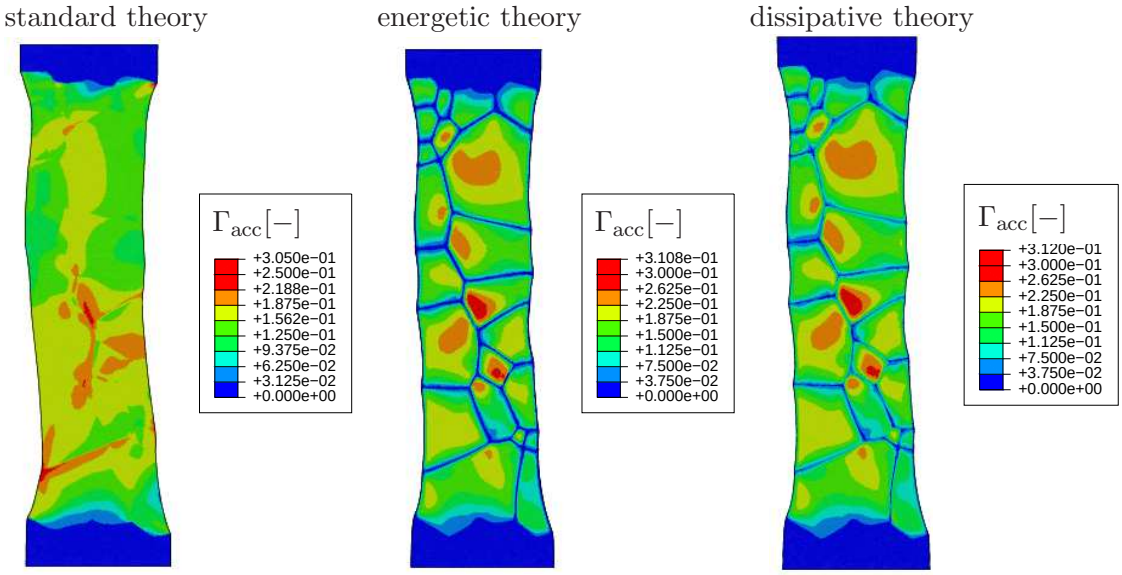

Figure 16: Oligocrystal, multiple slip: Γ_{acc}-distribution at $F_{11} = 1.1$ obtained with standard crystal plasticity theory, energetic and dissipative gradient theory.

hard boundary conditions lead to a stiffer response (see Figure 18) which restrict the deformation modes as well. Compared to the standard crystal plasticity theory, more deformation occurs within each grain. The micro-hard boundary conditions lead to a gradual decrease of the plastic slip towards the boundaries. Based on the orientations different distributions are observed in each grain. The boundary layers result in a stiffer behavior between the grains compared to the free surface of the standard crystal plasticity theory. This may explain why slight contractions are visible at the surface boundaries in several grains.

A strongly heterogeneous plastic slip distribution is visible, based on the orientations of the grains. The region of high activity in the standard crystal plasticity theory also represents the region of most activity in the energetic gradient crystal plasticity theory. The dislocation distribution displays typical behavior, in which the dislocations of greatest magnitude are seen near the boundaries. A high plastic slip gradient within a grain leads to a high dislocation density. For the full gradient theory, the distribution of the effective plastic slip γ_{eff} and of the dislocation distribution are similar to that of the energetic theory. The distribution as well as the magnitude of the plastic slip do not change significantly when compared with the energetic theory. Note that the size of each grain is significantly larger compared to the single crystal structure. The effect of the dissipative microstress is concentrated to the grain boundary solely, and, therefore, is relatively small for this sample. For the dislocation distribution no significant differences are visible as well.

The average stress-strain behavior is shown in Figure 18 which confirms the results from the

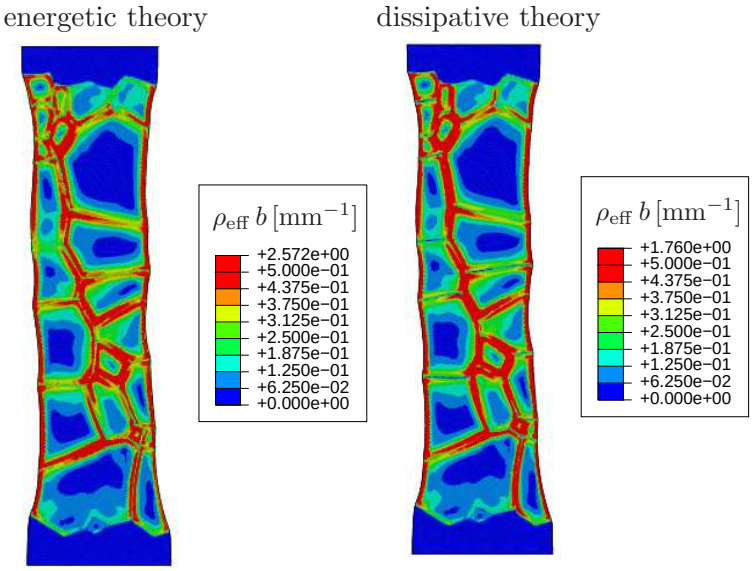

Figure 17: Oligocrystal, multiple slip: ρ_{eff}-distribution at $F_{11} = 1.1$ obtained with energetic and dissipative gradient theory.

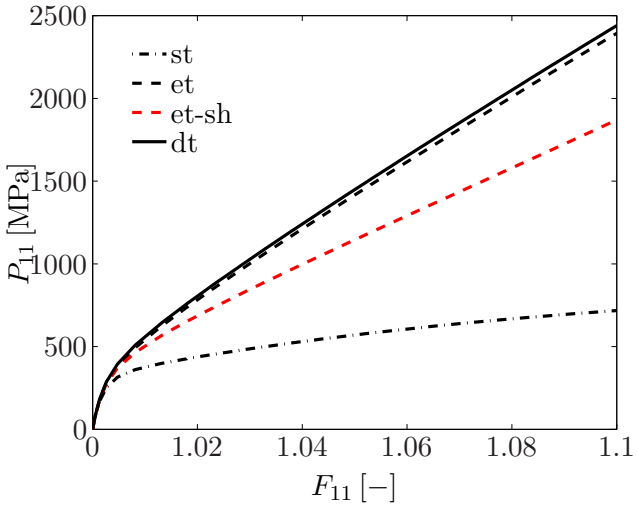

Figure 18: Oligocrystal, multiple slip: Comparison of macroscopic stress-strain behavior between standard crystal plasticity theory (st), energetic gradient crystal plasticity theory including self and latent hardening (et), energetic gradient crystal plasticity theory considering only self hardening (et-sh) and dissipative gradient theory (dt).

single crystal case. The standard crystal plasticity theory predicts the lowest stress level. The effect of latent hardening is seen as well by comparing the two cases for the energetic theory including self and latent hardening as well as self hardening only.

6 Summary

The objective of this investigation has been, first, to extend to the large-deformation and viscoplastic case the hardening model for strain-gradient single-crystal plasticity developed by Gurtin and Reddy [26]. An algorithm for the solution of the corresponding finite element approximation has been implemented, and explored numerically via selected examples. The algorithm is based on a dual-mixed approach in which the gradient of plastic slip rate is treated as a global variable while the slip rate is solved for locally. This algorithm easily accommodates the new hardening relations.

Numerical results have been presented for the standard crystal plasticity theory as a benchmark, and for the gradient theory for both the solely energetic case as well as that with energetic and dissipative effects present. The examples treated include single- and polycrystals, with various combinations of single and multiple slip, as well as self- and latent-hardening.

Latent hardening is seen to strongly influence the behavior. Likewise, the inclusion of dissipative gradient effects through the microstress has a pronounced effect on material behavior for models in which the domain size is small relative to the gradient length-scale. On the other hand, for large samples the effect is minimal. Overall, the hardening relation captures interaction between slip systems effectively, while being simple in structure.

Appendix

The standard, the energetic and full gradient crystal plasticity theories yield non-linear governing equations which are solved with the help of a Newton–Raphson method. For the discretization a semi-discretization technique has been applied: In space, finite elements are used while in time, the algorithmic formulation of the above model relation is based on the following backward Euler time integration of $\dot{\boldsymbol{F}}_P = \boldsymbol{L}_P \cdot \boldsymbol{F}_P$ over a time interval $[t_n, t_{n+1}]$:

$$\frac{1}{\Delta t_{n+1}} \left[\boldsymbol{I} - \boldsymbol{F}_{\mathrm{P}\,n} \cdot \boldsymbol{F}_{\mathrm{P}\,n+1}^{-1} \right] = \sum_\alpha \nu_{\alpha\,n+1}\, \boldsymbol{s}_\alpha \otimes \boldsymbol{n}_\alpha \,. \tag{45}$$

$\boldsymbol{F}_{\mathrm{e}\,n+1}$ is calculated via

$$\boldsymbol{F}_{\mathrm{e}\,n+1} = \boldsymbol{F}_{\mathrm{e}\,n+1}^{\mathrm{tr}} \cdot \left[\boldsymbol{I} - \Delta t_{n+1} \sum_\alpha \nu_{\alpha\,n+1}\, \boldsymbol{s}_\alpha \otimes \boldsymbol{n}_\alpha \right] , \tag{46}$$

where $\boldsymbol{F}_{\mathrm{e}\,n+1}^{\mathrm{tr}} = \boldsymbol{F}_{n+1} \cdot \boldsymbol{F}_{\mathrm{p}\,n}^{-1} = \boldsymbol{F}_{n+1} \cdot \boldsymbol{F}_n^{-1} \cdot \boldsymbol{F}_{\mathrm{e}\,n}$. The corresponding stress algorithm is based on the Green measure $\boldsymbol{E}_{\mathrm{e}\,n+1} = \frac{1}{2} \left[\boldsymbol{F}_{\mathrm{e}\,n+1} \cdot \boldsymbol{F}_{\mathrm{e}\,n+1} - \boldsymbol{I} \right]$ of elastic strain. The stress algorithm is

completed by the calculation of the different stress measures

$$\begin{aligned} \boldsymbol{S}_{\mathrm{e}\,n+1} &= \lambda\,\mathrm{tr}(\boldsymbol{E}_{\mathrm{e}\,n+1})\boldsymbol{I} + 2\mu\,\boldsymbol{E}_{\mathrm{e}\,n+1}, \\ \boldsymbol{M}_{\mathrm{e}\,n+1} &= \boldsymbol{F}_{\mathrm{e}\,n+1}^{\mathrm{T}} \cdot \boldsymbol{F}_{\mathrm{e}\,n+1} \cdot \boldsymbol{S}_{\mathrm{e}\,n+1}\,, \\ \boldsymbol{P}_{n+1} &= \boldsymbol{F}_{\mathrm{e}\,n+1} \cdot \boldsymbol{S}_{\mathrm{e}\,n+1} \cdot \boldsymbol{F}_{\mathrm{p}\,n+1}^{-\mathrm{T}}\,, \\ \tau_{\alpha\,n+1} &= \boldsymbol{s}_\alpha \cdot \boldsymbol{M}_{\mathrm{e}\,n+1} \cdot \boldsymbol{n}_\alpha. \end{aligned} \tag{47}$$

In case of the standard crystal plasticity theory, the plastic slip rate is determined via

$$\nu_{\alpha\,n+1} = \frac{1}{t_{\star,\alpha}} \left[\frac{|\tau_{\alpha\,n+1}|}{S_{\alpha\,n+1}} \right]^{\frac{1}{m_0}} \mathrm{sign}(\tau_{\alpha\,n+1}). \tag{48}$$

In case of the gradient theory, the plastic slip rate is determined via

$$\nu_{\alpha\,n+1} = \frac{1}{t_{\star,\alpha}} \left[\frac{|\tau_{\alpha\,n+1} + \mathrm{Div}\boldsymbol{\xi}_{\alpha\,n+1}|}{S_{\alpha\,n+1}} \right]^{\frac{1}{m_0}} \mathrm{sign}(\tau_{\alpha\,n+1} + \mathrm{Div}\boldsymbol{\xi}_{\alpha\,n+1}) \tag{49}$$

and the simplified version of the vector microstress is calculated as

$$\boldsymbol{\xi}^{\mathrm{en}}_{\alpha\,n+1} = -\boldsymbol{s}_\alpha b \sum_\beta l_\alpha\, l_\beta\, h_{\mathrm{g}0}[\chi_{\alpha\,\beta} + \iota_{\alpha\,\beta}]\, \varrho^{\mathrm{ge}}_{\beta\,n+1} \tag{50}$$

where $\rho^{\mathrm{ge}}_{\alpha\,n+1} = \rho^{\mathrm{ge}}_{\alpha\,n} + \Delta t_{n+1}\,\dot{\rho}^{\mathrm{ge}}_{\alpha\,n+1}$. The problem is solved applying a dual mixed approach: the displacement and the GND density $\dot{\rho}^{\mathrm{ge}}_{\alpha\,n+1} = -\frac{1}{b}\boldsymbol{s}_\alpha \cdot \nabla_{\boldsymbol{X}}\nu_{\alpha\,n+1}$ are solved for globally, whereas the slip rate ν_{n+1} is solved for locally.

The dissipative problem is handled accordingly - with the differences that on the global level the full gradient $\nabla_{\boldsymbol{X}}\nu_{\alpha\,n+1}$ is considered and that on the local level, not only the scalar-valued flow rule $(42)_1$ needs to be solved but also the vector-valued relation $(42)_2$ for the dissipative microstress $\boldsymbol{\xi}^{\mathrm{d}}_\alpha$. Both equations are highly non-linear and strongly coupled.

Acknowledgements

Part of this research was done while S.B. visited the Centre for Research in Computational and Applied Mechanics, University of Cape Town, whose hospitality is gratefully acknowledged. S.B. was supported by the German Science Foundation (DFG), contract PAK 250 (BA 3951/2), which is greatfully acknowledged.
B.D.R. was supported through the South African Research Chair in Computational Mechanics by the Department of Science and Technology and the National Research Foundation. This support is gratefully acknowledged.

References

[1] L. Anand, M. E. Gurtin, S. P. Lele, and C. Gething. A one-dimensional theory of strain-gradient plasticity: Formulation, analysis, numerical results. *JMPS*, 53:1789–1826, 2005.

[2] L. Anand and M. Kothari. A computational procedure for rate-independent crystal plasticity. *JMPS*, 44:525–558, 1996.

[3] A. Arsenlis, D. M. Parks, R. Becker, and V. V. Bulatov. On the evolution of crystallographic dislocation density in non-homogeneously deforming crystals. *JMPS*, 52:1213 – 1246, 2004.

[4] R. Asaro. Crystal plasticity. *Journal of Applied Mechanics ASME*, 50:921–934, 1983.

[5] R. Asaro and A. Needleman. Texture development and strain hardening in rate dependent polycrystals. *Acta Metallurgica*, 33(6):923 – 953, 1985.

[6] M. F. Ashby. The deformation of plastically non-homogeneous materials. *Philosophical Magazine*, 21:399–424, 1970.

[7] L. Bardella and A. Giacomini. Influence of material parameters and crystallography on the size effects describable by means of strain gradient plasticity. *Journal of the Mechanics and Physics of Solids*, 56:2906–2934, 2008.

[8] L. Bardella, J. Segurado, A. Panteghini, and J. Llorca. Latent hardening size effect in small-scale plasticity. *Model. Sim. Materials Science Eng.*, 21:055009, 2013.

[9] S. Bargmann and M. Ekh. Microscopic temperature field prediction during adiabatic loading in a gradient extended crystal plasticity theory. *IJSS*, 50:899–906, 2013.

[10] S. Bargmann, M. Ekh, K. Runesson, and B. Svendsen. Modeling of polycrystals with gradient crystal plasticity: A comparison of strategies. *Phil. Mag.*, 90:1263–1288, 2010.

[11] S. Bargmann and B. D. Reddy. Modeling of polycrystals using a gradient crystal plasticity theory that includes dissipative microstresses. *Eur. J. Mech. A/Solids*, 30:719–730, 2011.

[12] S. Bargmann, B. Svendsen, and M. Ekh. An extended crystal plasticity model for latent hardening in polycrystals. *Computational Mechanics*, 48:631–648, 2011.

[13] V. V. Bulatov, L. L. Hsiung, M. Tang, A. Arsenlis, M. C. Bartelt, W. Cai, J. N. Florando, M. Hiratani, M. Rhee, G. Hommes, T. G. Pierce, and T. D. de la Rubia. Dislocation multi-junctions and strain hardening. *Nature*, 440(7088):1174–1178, Apr. 2006.

[14] S. Conti and M. Ortiz. Dislocation microstructures and the effective behavior of single crystals. *Archive for Rational Mechanics and Analysis*, 176(1):103–147, 2005.

[15] M. Ekh, S. Bargmann, and M. Grymer. Influence of grain boundary conditions on modeling of size-dependence in polycrystals. *Acta Mechanica*, 218:103–113, 2011.

[16] M. Ekh, M. Grymer, K. Runesson, and T. Svedberg. Gradient crystal plasticity as part of the computational modeling of polycrystals. *Int. J. Num. Meth. Eng.*, 72:197–220, 2007.

[17] L. P. Evers, W. A. M. Brekelmanns, and M. G. D. Geers. Non-local crystal plasticity model with intrinsic ssd and gnd effects. *JMPS*, 52:2379–2401, 2004.

[18] N. A. Fleck and J. W. Hutchinson. A reformulation of strain gradient plasticity. *Journal of the Mechanics and Physics of Solids*, 49:2245–2271, 2001.

[19] H. Gao and Y. Huang. Geometrically necessary dislocation and size-dependent plasticity. *Scripta Materialia*, 48(2):113 – 118, 2003.

[20] M. Gurtin, L. Anand, and S. P. Lele. Gradient single-crystal plasticity with free energy dependent on dislocation densities. *Journal of the Mechanics and Physics of Solids*, 55:1853–1878, 2007.

[21] M. E. Gurtin. On the plasticity of single crystals: free energy, microforces, plastic-strain gradients. *Journal of the Mechanics and Physics of Solids*, 48:989–1036, 2000.

[22] M. E. Gurtin. A theory of viscoplasticity that accounts for geometrically necessary dislocations. *Journal of the Mechanics and Physics of Solids*, 50:5–32, 2002.

[23] M. E. Gurtin. A theory of grain boundaries that accounts automatically for grain misorientation and grain-boundary orientation. *Journal of the Mechanics and Physics of Solids*, 56:640–662, 2008.

[24] M. E. Gurtin and L. Anand. A theory of strain gradient plasticity for isotropic, plastically irrotational materials. Part II: Finite deformations. *International Journal of Plasticity*, 21:2297–2318, 2005.

[25] M. E. Gurtin, E. Fried, and L. Anand. *The Mechanics and Thermodynamics of Continua*. Cambridge University Press, 2010.

[26] M. E. Gurtin and B. D. Reddy. Gradient single-crystal plasticity within a miseshill framework based on a new formulation of self- and latent-hardening. *Journal of the Mechanics and Physics of Solids*, (0):–, 2014.

[27] E. O. Hall. The deformation and ageing of mild steel: III discussion of results. *Proceedings Physical Society London B*, 64:747–753, 1951.

[28] M. Henning and H. Vehoff. Local mechanical behavior and slip band formation within grains of thin sheets. *Acta Materialia*, 53:1285–1292, 2005.

[29] J. W. Hutchinson. Elastic-plastic behaviour of polycrystalline metals and composites. *Proc. Roy. Soc. London. A*, 319(1537):247–272, 1970.

[30] B. Klusemann, B. Svendsen, and H. Vehoff. Modeling and simulation of deformation behavior, orientation gradient development and heterogeneous hardening in thin sheets with coarse texture. *International Journal of Plasticity*, 50(0):109–126, 2013.

[31] B. Klusemann, T. Yalcinkaya, M. Geers, and B. Svendsen. Application of non-convex rate dependent gradient plasticity to the modeling and simulation of inelastic microstructure development and inhomogeneous material behavior. *Computational Materials Science*, 80(0):51 – 60, 2013.

[32] S. P. Lele and L. Anand. A small-deformation strain-gradient theory for isotropic viscoplastic materials. *Philosophical Magazine*, 88:3655–3689, 2008.

[33] V. Levkovitch and B. Svendsen. On the large-deformation- and continuum-based formulation of models for extended crystal plasticity. *IJSS*, 43:7246–7267, 2006.

[34] S. Limkumnerd and E. van der Giessen. Statistical approach to dislocation dynamics: From dislocation correlations to a multiple-slip ontinuum theory of plasticity. *Physical Review B*, 77:184111–1841112, 2008.

[35] A. Needleman and J. G. Sevillano. Preface to the viewpoint set on: geometrically necessary dislocations and size dependent plasticity. *Scripta Materialia*, 48:109–111, 2003.

[36] C. F. Niordson and B. N. Legarth. Strain gradient effects on cyclic plasticity. *Journal of the Mechanics and Physics of Solids*, 58:542–557, 2010.

[37] W. Nix and H. Gao. Indentation size effects in crystalline materials: a law for strain gradient plasticity. *Journal of the Mechanics and Physics of Solids*, 46:411–425, 1998.

[38] F. Norton. *Creep of Steel at High Temperatures*. McGraw-Hill, New York, 1929.

[39] J. F. Nye. Some geometric relations in dislocated crystals. *Acta Metall.*, 1:153–162, 1953.

[40] D. Peirce, R. Asaro, and A. Needleman. An analysis of nonuniform and localized deformation in ductile single crystals. *Acta Metallurgica*, 30(6):1087 – 1119, 1982.

[41] N. J. Petch. The cleavage strength of polycrystals. I. *Journal of Iron and Steel Institute*, 174:25–28, 1953.

[42] T. M. Povall, A. T. McBride, and B. D. Reddy. Finite element simulation of large-strain single-crystal viscoplasticity: an investigation of various hardening relations. *Comp. Mat. Sci.*, 81:386–396, 2013.

[43] B. D. Reddy. The role of dissipation and defect energy in variational formulations of problems in strain-gradient plasticity. Part 2: Single-crystal plasticity. *Continuum Mechanics and Thermodynamics*, 23:551–572, 2011.

[44] B. D. Reddy. Some theoretical and computational aspects of single-crystal strain-gradient plasticity. *Zeitschrift für angewandte Mathematik und Mechanik (ZAMM)*, 93:844–867, 2013.

[45] B. D. Reddy. Variational formulations for single-crystal strain- gradient plasticity at large deformations. *GAMM Mitteilungen*, 36(2):149–160, 2013.

[46] J. Y. Shu and N. A. Fleck. Strain gradient crystal plasticity: size-dependent deformation of bicrystals. *Journal of the Mechanics and Physics of Solids*, 47:297–324, 1999.

[47] G. Z. Voyiadjis and B. Beliktas. Mechanics of strain gradient plasticity with particular reference to decomposition of the state variables into energetic and dissipative components. *International Journal of Engineering Science*, 47:1405–1423, 2009.

[48] S. Wulfinghoff and T. Böhlke. Equivalent plastic strain gradient enhancement of single crystal plasticity: theory and numerics. *Proc. Royal Soc. A*, 468(2145):2682–2703, 2012.

[49] T. Yalcinkaya, W. Brekelmans, and M. Geers. Non-convex rate dependent strain gradient crystal plasticity and deformation patterning. *IJSS*, 49(18):2625 – 2636, 2012.